

Dynamic stall life-cycle on a rotating blade in steady forward flight

Vrishank Raghav

Postdoctoral Fellow

Narayanan Komerath

Professor

School of Aerospace Engineering

Georgia Institute of Technology

Atlanta, GA

Abstract

Stereoscopic particle image velocimetry is used to study the three-dimensional flowfield over a retreating rotor blade in dynamic stall. The dynamic stall event is characterized from the inception of dynamic flow separation through dynamic reattachment on the rotating blade at one radial location. First, the separation event is studied by characterizing the dynamic separation mechanism in action and the effect of advance ratio on the onset of dynamic separation. Next, the vortex dynamics and the associated cycle-to-cycle variations during the dynamic stall event are characterized. The radial component of flow (from root to blade tip) during the dynamic stall event is shown to be significant in the rotating environment. Proper orthogonal decomposition is used to characterize the unsteady nature of the dominant flow structure. Comparisons of the phase-averaged and instantaneous velocity fields shows the dynamic stall vortex to be spatially diffused. These results imply significant effects on the pitching moment variation from cycle-to-cycle since the effective center of the vortex appears

Presented at the AHS 70th Annual Forum, Montreal, Quebec, Canada, May 20–22, 2014.

Corresponding author: komerath@gatech.edu

to occur at different locations in every cycle. Finally, the last phase of dynamic stall, the dynamic reattachment phase on the rotating blade is investigated. Dynamic reattachment was observed to be affected by advance ratio with an increase in advance ratio resulting in early dynamic reattachment.

Nomenclature

Γ	Circulation	m^2/s
Γ_1	Scalar function	
μ	Advance ratio	
Ω	Rotor angular velocity	rad/s
ω	Vorticity	$1/\text{s}$
ψ	Azimuth	deg
b	Span of the blade	m
c	Chord length of the blade	m
k	Reduced frequency	
R	Rotor disc radius	m
r	Local radial location	m
Re	Reynolds number based on chord and effective velocity	
U_∞	Freestream velocity	m/s
U_e	Effective velocity	m/s
U_r	Radial velocity	m/s
U_T	Blade tip speed	m/s
u, v, w	Velocity in x,y,z directions	m/s

Introduction

Dynamic stall (DS) occurs on lifting surfaces experiencing a rapid increase of the angle of attack beyond the static stall angle [1]. DS is accompanied by large excursions in lift and pitching moment, caused by the formation and convection of the dynamic stall vortex (DSV). Most of the literature on explaining and predicting DS arises from interest in operation of jet engine compressors at high stage pressure ratio, post-stall maneuvering of combat aircraft, rotorcraft forward flight at high advance ratio, and horizontal axis wind turbine operating at high yaw angles. In recent years, there is renewed interest in unsteady aerodynamics of rotating wings due to biologically inspired flight at low Reynolds numbers applied to unmanned air vehicles. While the insects use the DSV to improve their flight performance, the DSV hinders performance in cases such as compressors and helicopter rotors. Although DS has been studied extensively, predicting the precise timing, extent and hence the phase of a DS event, and reattachment on a rotating blade, remains elusive. Most experimental investigations of DS have been limited to two-dimensional flows over oscillating airfoils in wind and water tunnels [1, 2] and on oscillating finite wings [3, 4]. Computational fluid dynamics investigations have progressed from inviscid formulations to full Navier-Stokes simulations. However, the occurrence of DS is influenced by three-dimensional effects such as viscous interactions associated with rotational augmentation, as well as inviscid ones including finite wing and local yaw effects. Reactive centrifugal effects are expected to drive a strong radial flow [5] and the coupled effects of centrifugal and Coriolis forces in the rotating environment add more complexity to the flow characteristics.

Several experimental investigations have analyzed pressure distribution data over a rotating lifting surface during DS. Ham [6], McCroskey [7], Bousman [8] have gathered pressure measurements on a rotating helicopter blade during DS conditions. Butterfield [9], Shreck and Robinson [10] have gathered similar pressure measurement data on rotating wind turbine blades in yawed configurations. A few investigations have analyzed velocity measurements gathered using constant temperature anemometry and laser Doppler velocimetry which are single point velocity measurement techniques. An improvement over the single point measurement technique is to acquire instantaneous velocity field data which allow for a better interpretation of kinematics and dynamics of the flow features. Global velocity field measurements on

oscillating airfoils/wings have been conducted by using techniques like Particle Image Velocimetry (PIV) in several investigations [11–13].

Hitherto, there exists few studies which have investigated the flow field level details of DS on rotating configurations. Fujisawa [14] and Ferreira [15] have used PIV to investigate the flow field details of DS on rotating blades. In these experiments the rotating blades were set up to operate as a vertical axis wind turbines, where the effect of reactive centrifugal forces act perpendicular to the blade planform, unlike on rotating helicopter or horizontal axis wind turbine blades where they act along the span of the blade. Rotating flat plates with fixed pitch at low Reynolds numbers have been studied recently in the light of insect wing aerodynamics [16, 17]. But none of these investigations applied to insect wings incorporate simultaneously rotating and pitching wings in forward flight. Recently, rotating helicopter rotor blades have been used to experimentally study the flow field details of DS [18–20]. References [18–20] report significant radial flow observed in the core of the DSV and Raghav discusses the radial destabilization of the vortex position at outboard radial locations.

Scope and objectives

This work is an extension of Raghav [20] where the variation of the DS event with radial location was investigated at one azimuth ($\psi = 270^\circ$) and advance ratio of $\mu = 0.33$ using planar PIV. In this work, experiments are conducted on a two-bladed teetering rotor in steady forward flight in a low speed wind tunnel. Stereoscopic Particle Image Velocimetry (SPIV) is used to gather three-dimensional velocity field data on the rotating blade in DS conditions. For the first time, flow field details from the inception of dynamic flow separation through the dynamic flow reattachment phase of the flow during a dynamic stall event on a rotating blade is investigated. In order to capture the DS life-cycle, measurements are acquired at several azimuthal locations where DS is expected to occur on a rotor in steady forward flight. In addition, measurements were acquired at three radial locations and three advance ratios conditions to further characterize variations in the DS event. However, in order to discuss the dynamic stall life-cycle in detail, flow field details of only one radial location ($r/R = 0.6$) are used in this paper.

Methodology

Experimental setup and flow conditions

The experiments were conducted in the high advance ratio facility (see Fig. 1) setup in the test section of the John Harper 2.13m×2.74m low speed wind tunnel at the Georgia Institute of Technology [18–20]. The high advance ratio facility was modified prior to the current experiments by incorporating a new set of high speed ball bearings to reduce the vibrations of the rotor at high operating speeds. The motor was positioned below the rotor and in order to simplify the operations a teetering rotor with manually adjustable collective and cyclic pitch was preferred. A rectangular (non-tapered) blade with zero twist and aspect ratio of 3.49 was used in the investigation. The blade used in this work has a static stall angle of 13°, please see [21] for more details on the static aerodynamic characteristics of the blade used in this investigation. Further details of the high advance ratio rotor facility specifications are provided in Table 1. A photo-micro sensor was installed on the rotor to enable phase locked data measurement. The motor for the closed circuit wind tunnel was upgraded in 2013 and is now powered by a three-phase 600 hp induction motor controlled by a variable frequency drive. The upgraded drive is a closed loop controller with 0.1% error in motor speed setting, resulting in superior control over the steady state velocity. As a result the freestream longitudinal turbulence intensity at the entrance of the empty test section of the wind tunnel is under 0.06 %. The turbulence intensity was measured at a freestream velocity of 34 m/s using velocity fluctuation data gathered using a hot-film conditioned with a 3 Hz high pass filter and 2.5 kHz low pass filter before the data was digitized.

In order to study the DS event on the retreating rotor blade, a rotor angular velocity $\Omega = 20.94$ rad/s was chosen which yields a tip velocity $U_T = 18.62$ m/s. The experiments were performed at three freestream velocities $U_\infty = 4.65, 6.7, 7.44$ m/s non dimensionalized as advance ratios $\mu = \frac{U_\infty}{U_T} = 0.25, 0.36$ and 0.4, respectively. The azimuthal variation of pitch angle was controlled using the swashplate which prescribed the pitch angle given by the expression: $\theta(\psi) = \theta_o + \theta_c \sin \psi$. A collective pitch of $\theta_o = 10^\circ$ and a longitudinal cyclic of $\theta_c = -5^\circ$ were used to create a pitch angle of $\theta = 15^\circ$ on the retreating blade at $\psi = 270^\circ$. This combination of collective and cyclic pitch angles is sufficient to induce dynamic stall as demonstrated by DiOttavio et al. [18] using flow visualization and verified by Raghav [20] by using PIV

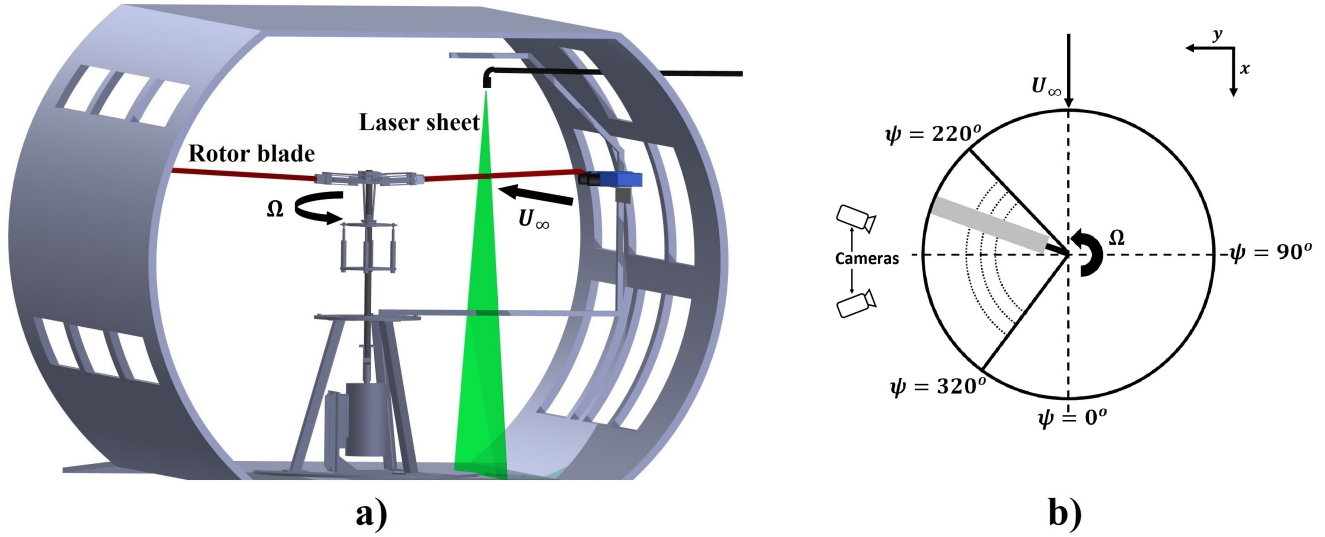


Fig. 1 Illustration of the rotor setup in the low speed wind tunnel. a) View from upstream of the test section. b) Top view of the rotor showing measurement locations

measurements. The chordwise velocity measurements were made at three radial locations $r/R = 0.5, 0.6, 0.7$ (see Fig. 1b). Each combination of radial location, azimuthal angle, and advance ratio is associated with its reduced frequency ($k = \frac{\Omega c}{2U_e}$) and Reynolds number based on chord length ($Re = \frac{U_e c}{\nu}$), where $U_e|_\psi = U_T \frac{r}{R} + U_\infty \sin\psi$ is the effective velocity, and ψ is the azimuthal angle defined in Fig. 1b. The angle of attack at each azimuthal location was defined as $\alpha(\psi) = \theta(\psi) + \tan^{-1} \frac{v_i}{U_e}$, where v_i is the induced velocity at each flow condition. Induced velocity was measured as the axial component of the velocity field at each flow condition when the blade was upstream of the measurement location. In order to discuss the dynamic stall life-cycle in detail, in this paper, we focus on one radial location of $r/R = 0.6$ and two advance ratios $\mu = 0.36, 0.40$. The azimuthal angles at which measurements were acquired in this work with their corresponding Reynolds number, reduced frequencies and angle of attack are summarized in Table 2.

SPIV instrumentation

The coupled effects of reactive centrifugal forces and Coriolis forces in the rotating environment make DS a highly three-dimensional event. Hence, there is a need to understand the span-wise (radial) flow

during the DS event. In order to bridge this gap in knowledge, SPIV was used to investigate the flow field on the rotating blade. The illumination was provided by a double-cavity Nd:YAG laser with a pulse energy of 200 mJ. The resulting beam diameter was about 2 mm with a pulse width of 5ns. A laser arm (a covered beam path) was used to deliver the laser beam to the measurement plane. Sheet optics was used at the end of the laser arm to generate a light sheet of 2 mm thickness. The flow was continuously seeded with approximately $10\mu\text{m}$ droplets generated by a Laskin-nozzle type indigenous aerosol generator.

McAlister [22] showed that fifty pitch cycles yielded converged statistics in the case of force measurements during dynamic stall. Hence, drawing a similar parallel a series of 75-100 phase-locked image pairs were acquired at each measurement location using PRO-X 2M cameras which have a 1600×1200 pixel resolution and a pixel size of $7.4\times 7.4\mu\text{m}^2$. Due to limited optical access, the angle of the two cameras for the stereo-PIV setup was limited to 20° (the errors introduced due to this are computed in the accuracy estimates section). The particle size in the camera image ranged from 1.76 pixels to 2.81 pixels. The focal length of the lens system was 50 mm and the aperture on the camera was set at f/8. In order to improve the signal to noise ratio of the PIV data, the blade was coated with Rhodamine paint and a bandpass filter ($532\pm 10\text{nm}$) was used on the camera to minimize laser reflections from the upper surface of the blade. In addition, the unavoidable laser reflections were masked during the velocity vector computations.

DaVis 8.0 software provided by LaVision was used to process the PIV data, the velocities were calculated from the spatial cross-correlation of the images. An interrogation window overlap of 50% and a second interrogation pass with a reduced window size was used to increase the signal-to-noise ratio of the correlation peak. The first pass utilized an interrogation window of 64×64 pixels while a 32×32 pixel window was used on the second pass. This yielded a spatial resolution between velocity vectors of $1.8\text{ mm}-2.1\text{ mm} \sim 0.01c-0.012c$ (note that due to laser reflections at the surface of the wing, the first discernible velocity vector was around 2.5 mm away from the surface of the wing). Post-processing of the vector images consisted of an applied vector range and a median filter. These greatly reduced the noise due to erroneous vectors appearing at the edges of the camera viewing window.

Accuracy estimates

The uncertainty in flow conditions resulted in a Reynolds number uncertainty of ± 468 . The uncertainty in pitch angle settings measured using a digital protractor and the phase-locking of the rotor estimated by image processing were both determined to be $\pm 0.05^\circ$. The blade used in the experimental investigation was comprehensively characterized to test the validity of the airfoil profile. The root mean square error of the difference from NACA0013 was less than 0.1% of the chord length.

The accuracy of the velocity measurements was computed using procedures outlined in Raffel [23]. Bias error for in-plane velocity (u, v) was determined by plotting the probability density histograms of the velocity field data, with a resolution of 0.01 m/s the histograms did not reveal any peak-locking error. The seeding particle lag error for in-plane velocity was estimated to be insignificant by considering the relaxation time of the seed particles to sharp changes in velocity. A transient solution for the response time of the seed particles ($10\mu\text{m}$) to a step change in velocity was determined. A comparison of the fluid time scale in the unsteady flow over a rotor blade to the response time of the particle showed that the fluid time scale was around 5-10 times the response time, indicating that the particle lag error was insignificant. Please refer to Raghav [24] for further details on the quantification of lag error due to oil droplet size. The random error for in-plane velocity measurement was between 0.4% and 1.2% of the maximum in-plane velocity ($U_p = 12.1$ m/s). Please refer to Raghav [20, 24] for further details on in-plane velocity measurement uncertainty.

The out-of-plane velocity (w) measurement uncertainty depends on the angle between the two cameras used in the SPIV. Lawson [25] suggests that the optimal angle is between $20^\circ - 30^\circ$, however, due to limited optical access the angle in this study was limited to 20° . The resulting random error for the out-of-plane velocity measurement was between 0.58% and 3.08% of the maximum out-of-plane velocity ($W_p = 9.1$ m/s). It should be noted that the random errors presented here are percentages based on the maximum values of two separate velocity components. All the uncertainties in velocity measurements are summarized in Table 3.

Results

In all the PIV vector fields presented in this work, the axes of the camera images are fixed in the wind tunnel coordinate system and have not been corrected for the pitch angle of the blade. A right-hand coordinate system is chosen with the origin $(x,z) = (0,0)$ at the leading-edge of the blade in all the vector fields. The x axis is positive to the right, the z axis is positive downwards and the y axis positive out-of-plane of the paper completing the right-handed coordinate system. The x and z dimensions are normalized by chord length, where $x/c = 0$ is the leading-edge and $x/c = -1$ is the trailing edge of the blade. While, the radial dimension y which represents the local radius in the right hand coordinate system is non-dimensionalized by tip radius (disc radius) R . In addition, for better visualization and analysis the corresponding freestream velocity component has been subtracted from the velocity vector fields. With the y axis as defined, out-of-plane velocity is positive and it indicates the flow towards the tip of the blade. Conversely, negative out-of-plane velocity indicates a radially inward flow towards the root of the blade.

The results section is organized as follows: first, the onset of dynamic flow separation on the rotating blade in forward flight is discussed. This is followed by a discussion of the DS event with respect to the DSV evolution, radial flow and cycle-to-cycle or (CTC) variations (including POD analysis). Finally, the dynamic flow reattachment phase of the DS event is discussed.

Dynamic separation

Predicting the precise timing of the dynamic stall event on a rotating blade is challenging. Typically, the stall initiation is a localized three-dimensional phenomenon, even if the blade itself has zero sweep and taper, and is not rotating. Hence, there has been considerable focus on identifying the physics of the separation delay and onset of dynamic stall. The mechanisms of dynamic stall onset and dynamic separation proposed in the literature are the following: *a*) classic trailing edge separation [1], *b*) shock induced separation [26], and *c*) bursting of a separation bubble [27]. In this section, we use phase-averaged velocity field data (average of phase-locked velocity field data) to derive insight into the separation mechanisms. The current experiments are conducted at low Mach numbers and hence we can say that the shock-induced separation mechanism does not play a role in these experiments. However, the other two

mechanisms a) and c) could be manifesting themselves in the current experiments. Classical trailing edge separation would be easier to identify, since it is a progressive mechanism and has a slow onset time. However, since the bursting of the separation bubble is a random event and presumably has a significant cycle-to-cycle (CTC) variation, the role of this mechanism in the dynamic separation event would be harder to ascertain.

Fig. 2 illustrates the phase-averaged velocity field streamlines overlaid on iso-vorticity contours for the retreating blade at $\psi = 220^\circ - 230^\circ$, $r/R = 0.6$, and $\mu = 0.36, 0.4$. Clearly, the flow close to the trailing edge has separated, evidenced by the reversal of flow close to the surface of the wing for $x/c \leq -0.4$ at $\psi = 220^\circ$. This is firm evidence that the dynamic stall mechanism in operation on the retreating rotor blade in these experiments is the classical trailing edge stall mechanism. A primary difference that can be observed is that with the increase in advance ratio the trailing edge separation has progressed towards the leading-edge. In other words at higher advance ratio ($\mu = 0.4$) the trailing edge separation onset occurs at an earlier azimuth when compared to the lower advance ratio ($\mu = 0.36$). The higher advance ratio results in a decrease in Reynolds number and an increase in reduced frequency. The coupled effects of such a change could be the reason for the earlier separation observed.

In this work, onset of DS was defined as the point where leading-edge separation is first observed. At $\psi = 230^\circ$ and $\mu = 0.36$ the trailing edge separation has progressed further towards the leading-edge ($x/c \leq -0.13$), but not yet resulted in leading-edge separation. However, at $\psi = 230^\circ$ and $\mu = 0.40$ complete leading-edge separation is observed, including evidence of a nascent DSV. While phase-averaged velocity fields provide a useful insight to the onset of DS event. Further analysis of the instantaneous velocity fields is necessary to ascertain any indications of a bursting separation bubble. Analysis of the instantaneous velocity fields indicates cycle-to-cycle variations in the flow fields. There were instances when no indication of separation was observed in the PIV velocity fields, while others showed clear evidence of separated flow (not shown in the paper). Further rigorous analysis needs to be performed to verify the separation mechanism in action in the current experiments.

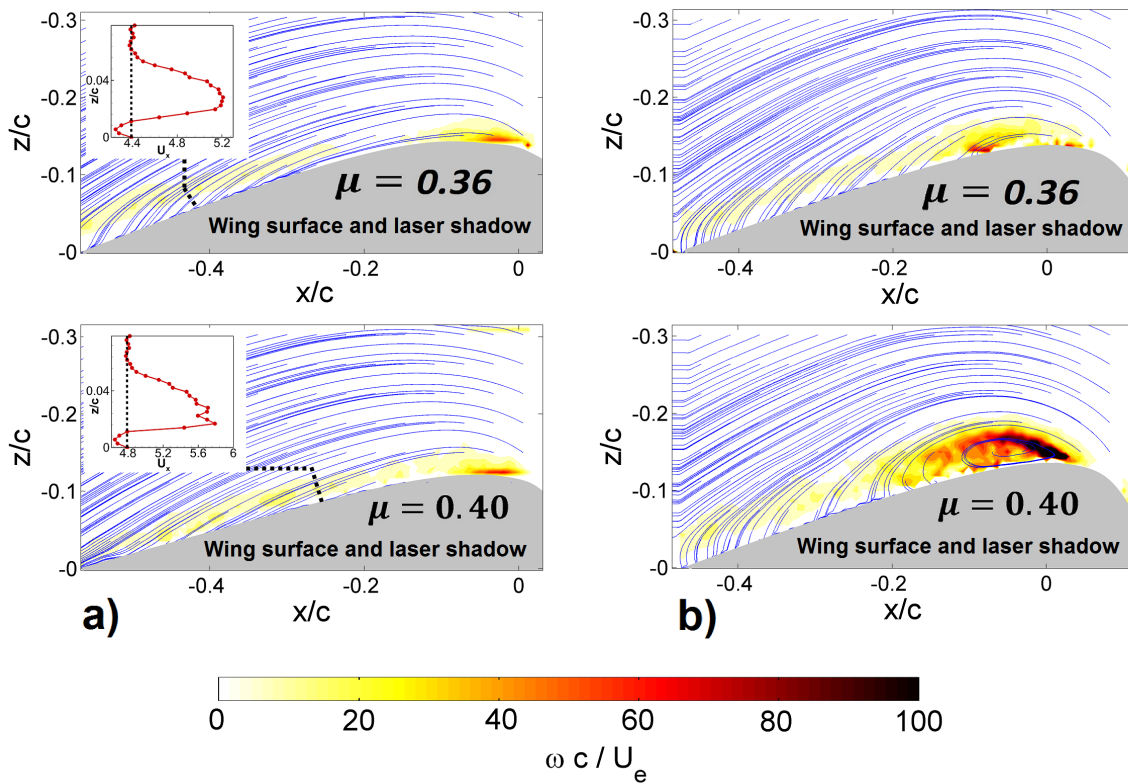


Fig. 2 Inception of separation observed for two advance ratios at $r/R = 0.6$: a) $\psi = 220^\circ$ and b) $\psi = 230^\circ$, the inset figure shows the variation of tangential velocity at the surface of the blade at the section marked by the dashed line. Wing and laser shadow shown in gray

DS life-cycle

DSV evolution

To effectively characterize the DSV a vortex center identification algorithm proposed by Graftieaux [28] was used to determine the location of the vortex. It is specifically designed to identify a large scale vortex superposed on a small-scale turbulent velocity field. The scalar function Γ_1 also called normalized angular momentum (NAM) is defined as

$$\Gamma_1(P) = \frac{1}{N} \sum_S \frac{(PM \wedge U_M) \cdot z}{\|PM\| \cdot \|U_M\|} = \frac{1}{N} \sum_S \sin(\theta_M) \quad (1)$$

where N is the number of points in the two-dimensional neighborhood S of any given point P in the measurement plane. M lies in S and z is the unit vector normal to the measurement plane. The parameter N plays the role a spatial filter, but affects the location of maximum Γ_1 weakly. This scalar function unlike gradient based vortex detection techniques does not require the evaluation of gradients and is hence less susceptible to experimental noise.

Fig. 3 summarizes the phase-averaged NAM plots at each azimuthal angle where data were gathered during the DS cycle (after inception of separation up to reattachment). As discussed earlier the onset of leading-edge separation at $r/R = 0.6$ and $\mu = 0.40$ was observed at $\psi = 230^\circ$. Shortly after the onset of separation at $\psi = 235^\circ$, a clear vortical structure is observed emanating from the leading-edge of the blade. The vortex appears elongated and pinned to the surface when compared to the two-dimensional DSV observations at similar Reynolds numbers and reduced frequencies [29]. As the azimuthal angle increases the vortex lifts off the blade surface and progresses to reach a maximum height above the surface of blade at $\psi = 270^\circ$, accompanied by further elongation of the vortex. Up until $\psi = 270^\circ$, the blade is undergoing the upstroke motion and reaches the maximum angle of attack at this azimuthal angle. Thereafter, the blade undergoes the downstroke motion, when the vortical structure is observed to recede towards the blade surface. During this phase the vortex also appears to “break-off” and shed vorticity, which is clearly observed in Fig. 3 at $\psi = 280^\circ$ and 290° . At $\psi = 290^\circ$ the vortex again appears pinned to the surface of the blade similar to what was observed at $\psi = 235^\circ$.

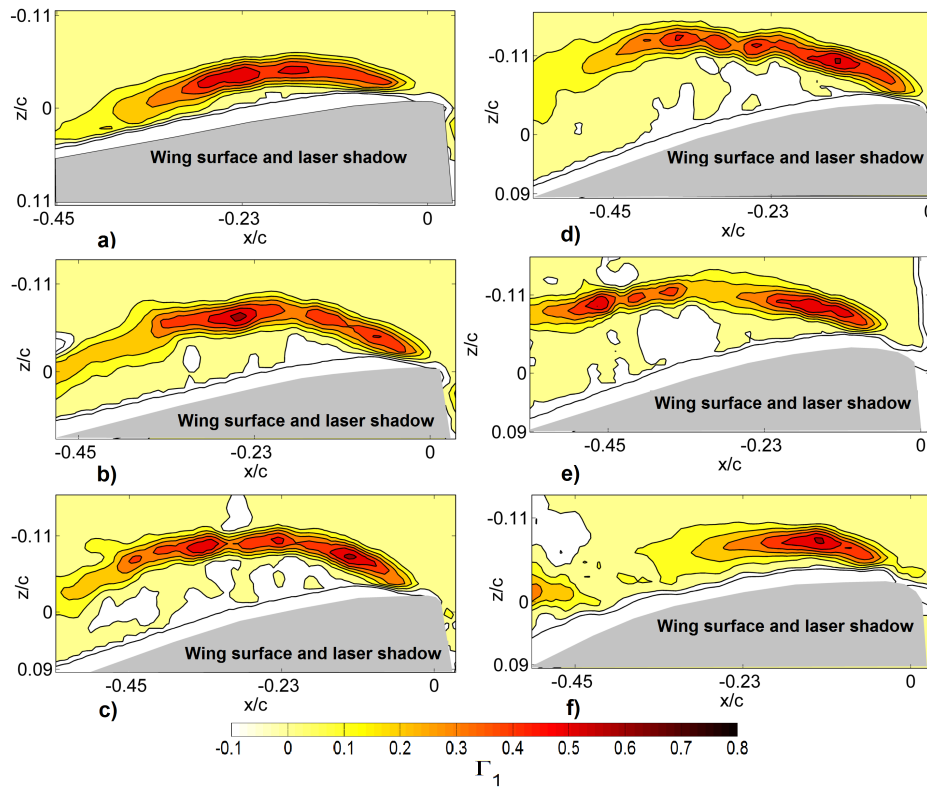


Fig. 3 NAM fields illustrating the DS cycle on a rotating blade at $r/R = 0.6$ and $\mu = 0.40$: $\psi =$ a) 235° , b) 252.6° , c) 262.6° , d) 270° , e) 280° , f) 290° . Wing and laser shadow shown in gray

Another salient feature of the DS cycle that is inferred from the NAM plots is the unsteadiness of the vortex (CTC variation). In the present experiments, velocity fields are captured once during each rotor revolution over the same blade (phase-locked data acquisition). As azimuthal angle increases (after onset of leading-edge separation) the value of Γ_1 has a maximum value at several locations within the phase-averaged vortex. The phase-averaged DSV presents itself as a spatially diffused vortical structure with multiple Γ_1 maximas. This is a clear indication that the CTC variations of the DSV are quite significant during the DS cycle. Qualitatively, a clear trend is observed in Fig. 3 with respect to the magnitude of CTC variations. The number of Γ_1 maximas increases with azimuthal angle up to the completion of upstroke ($\psi = 270^\circ$), the number then decreases due to the vortex shedding. Further qualitative analysis (POD analysis) and quantitative analysis of the CTC variations are discussed at a later stage in this section.

Radial flow

The coupled effects of reactive centrifugal forces and Coriolis forces in the rotating environment make DS a highly three-dimensional event. For example Raghav [19] demonstrated that the radial flow is of first order significance in the separated flow region during retreating blade dynamic stall. Hence, there is a need to understand the span-wise (radial) flow during the DS event. In order to specifically bridge this gap in knowledge, SPIV was used to investigate the flow field on the rotating blade. At every azimuthal angle the radial flow comprises of two components: a) yaw induced span-wise flow U_ψ and b) reactive centrifugal forces induced radial flow U_r . The total out-of-plane velocity at a given azimuthal angle could be expressed as $U_y = U_r + U_\psi$, where $U_\psi = U_\infty \cos\psi$, U_∞ is the freestream velocity, and ψ is the corresponding azimuthal angle at which the measurements are made. Since our objective here is to study the rotation induced radial flow, the total out-of-plane velocity has to be corrected for the yaw-induced span-wise velocity to yield the rotation induced radial flow as $U_r = U_y - U_\infty \cos\psi$. It should be noted that, the rotation induced radial flow component far away from the blade surface should be expected to maintain a value close to zero. Moreover, $\psi = 270^\circ$ is the only location where the span-wise (radial) flow is predominantly due to reactive centrifugal forces.

Fig. 4 illustrates the velocity vector fields overlaid on contours of the rotation induced radial flow for azimuthal angles $230^\circ \leq \psi \leq 310^\circ$ at $r/R = 0.6$ and $\mu = 0.4$ flow condition. With the right hand coordinate axes defined as x positive to the right and z positive downwards, a positive out-of-plane velocity indicates flow from the root to the tip of the blade and vice versa. At all the azimuthal angles there exists a region of positive radial velocity which indicates the flow from root to tip of the blade. The extent of radial flow over the upper surface of the rotating blade increases with azimuthal angle during the upstroke ($230^\circ \leq \psi < 270^\circ$) and decreases during the downstroke ($270^\circ < \psi \leq 310^\circ$). The extent of radial flow is the greatest at $\psi = 270^\circ$, which is also the azimuthal angle at which the most separation is observed and is the most unsteady (please refer to Fig. 3 and associated discussion). The separated flow region is clearly moving slower than the faster freestream and is hence greatly affected by reactive centrifugal forces.

Cycle-to-cycle (CTC) variations of DSV :

The analysis of the dominant behavior of a flow field with a large scale coherent structure superimposed on fine vortical structures is usually a challenge. An approach to define and identify coherent structures in a complex flow system is based on a proper orthogonal decomposition (POD) of the flow field. The technique denotes a procedure to represent a random spatio-temporal signal as a series of deterministic spatial functions with the temporal function as random coefficients. This modal bi-orthogonal decomposition is then used to approximate the original signal as accurately as possible based on an energy-weighted measure [30]. DaVis 8.1 a commercially available software was used to perform the POD analysis on the velocity fields. The software uses the snapshot technique described by Sirovich [31] to perform the analysis.

The POD technique was adopted to understand the dominant flow structure on a rotating blade during DS. As discussed earlier, POD assigns each spatial eigenmode an energy level, we first present and discuss the effect of advance ratio on the energy distribution between the modes of the flow. The lower modes usually represent the dominant structures of the flow field and are ascribed a higher energy level, while the higher modes represent the finer flow structures in the flow field and are associated with lower energy

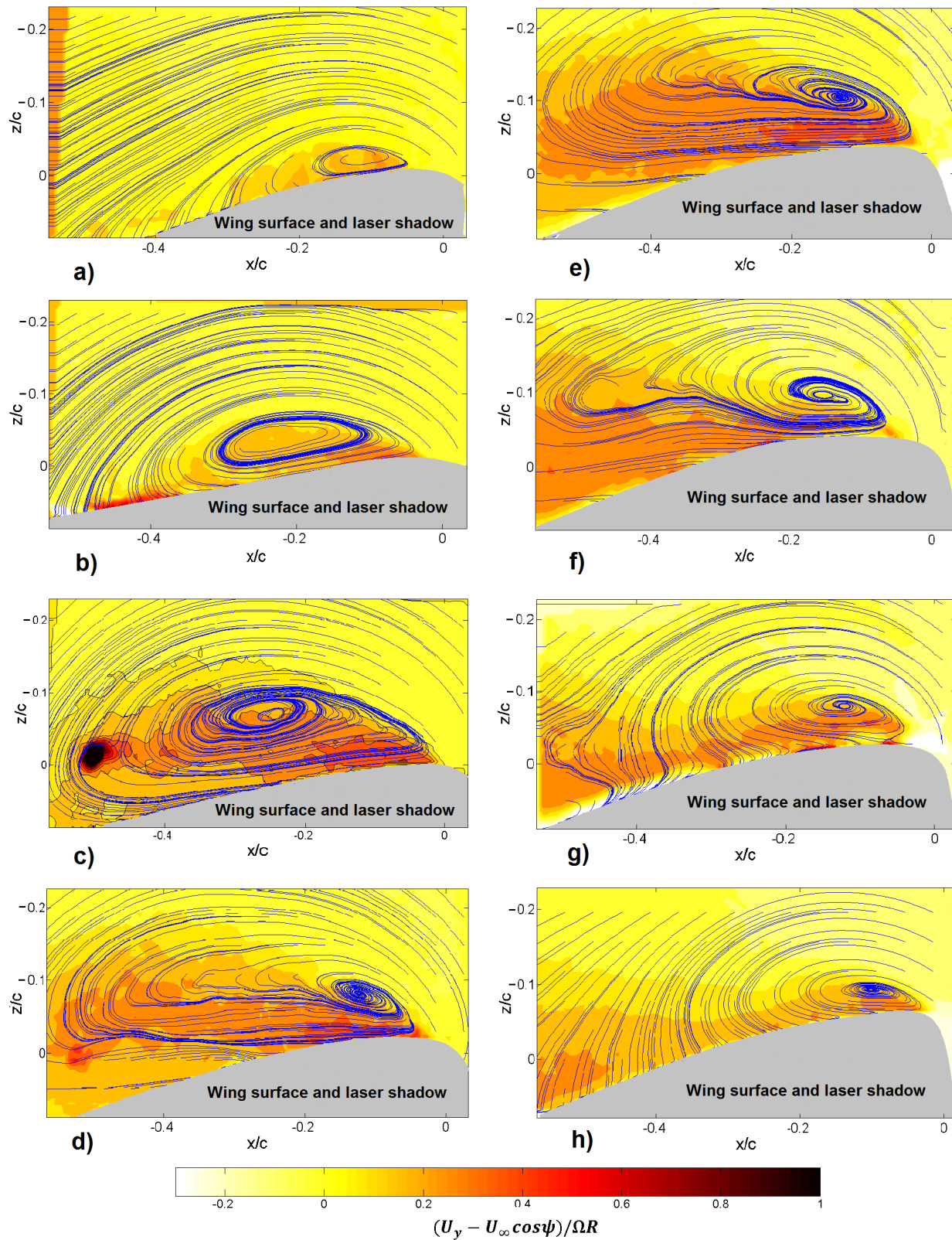


Fig. 4 Radial flow on the rotating blade during DS event at $r/R = 0.6$ and $\mu = 0.40$: $\psi =$ a) 230° , b) 235° , c) 252.6° , d) 262.6° , e) 270° , f) 280° , g) 290° , h) 310° . Wing and laser shadow shown in gray

levels. Fig. 5 illustrates the energy contained in each eigenmode of the flow at the measurement location $r/R = 0.6$. The inset is a zoomed in view of the same data to clearly differentiate between the energy levels of the lower modes. A change in advance ratio does not effect the energy content of the higher modes, however, the lower modes show a moderate change (5–10%) with advance ratio. Essentially, a variation in advance ratio affects only the dominant flow structures rather than the finer scale flow structures which are associated with lower energy levels. Hence, the approximated instantaneous flow field reconstructed using the first 3–4 eigenmodes should be sufficient to draw conclusions on the dominant behavior of the instantaneous flow field.

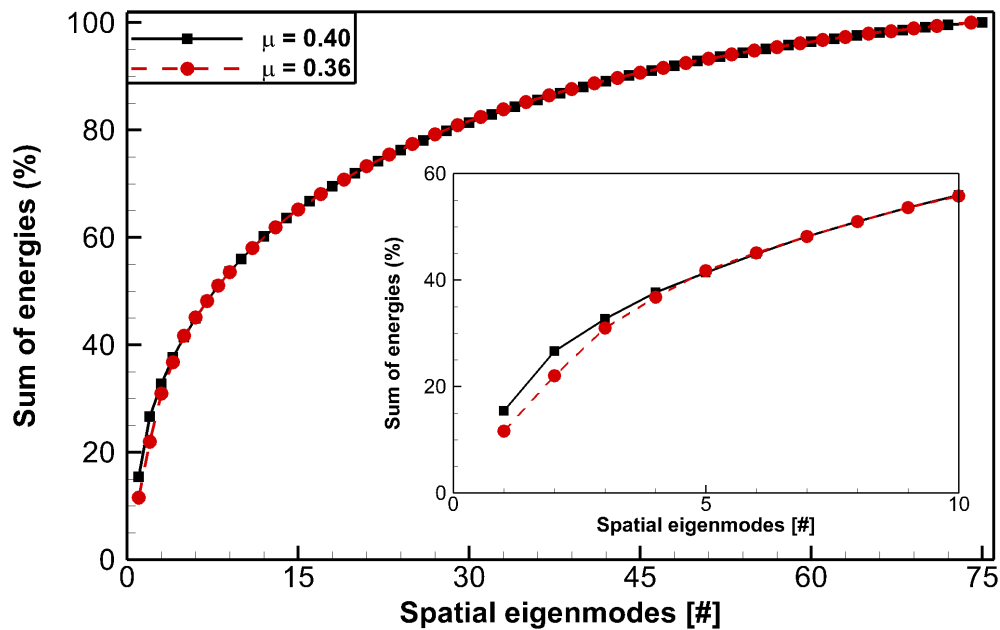


Fig. 5 Sum of energies associated with each eigenmode of the flow at $r/R = 0.6$ and $\psi = 270^\circ$

Fig. 6 depicts the unsteady behavior of the leading-edge shear layer by illustrating NAM fields of 10 consecutive rotations of the blade using the first 3 eigenmodes ($\sim 35\%$ energy). The shear layer in the approximated flow is observed to exhibit “oscillations”. However, this oscillatory nature of the shear layer disappears at low advance ratios and at inboard locations (not shown here for brevity). Hence, it can be concluded qualitatively that the dynamic stall vortex is observed to “jitter” at a combination of outboard radial location and higher advance ratio conditions tested in this work.

In order to quantify the CTC variations of the DSV, the variations due to other experimental artifacts

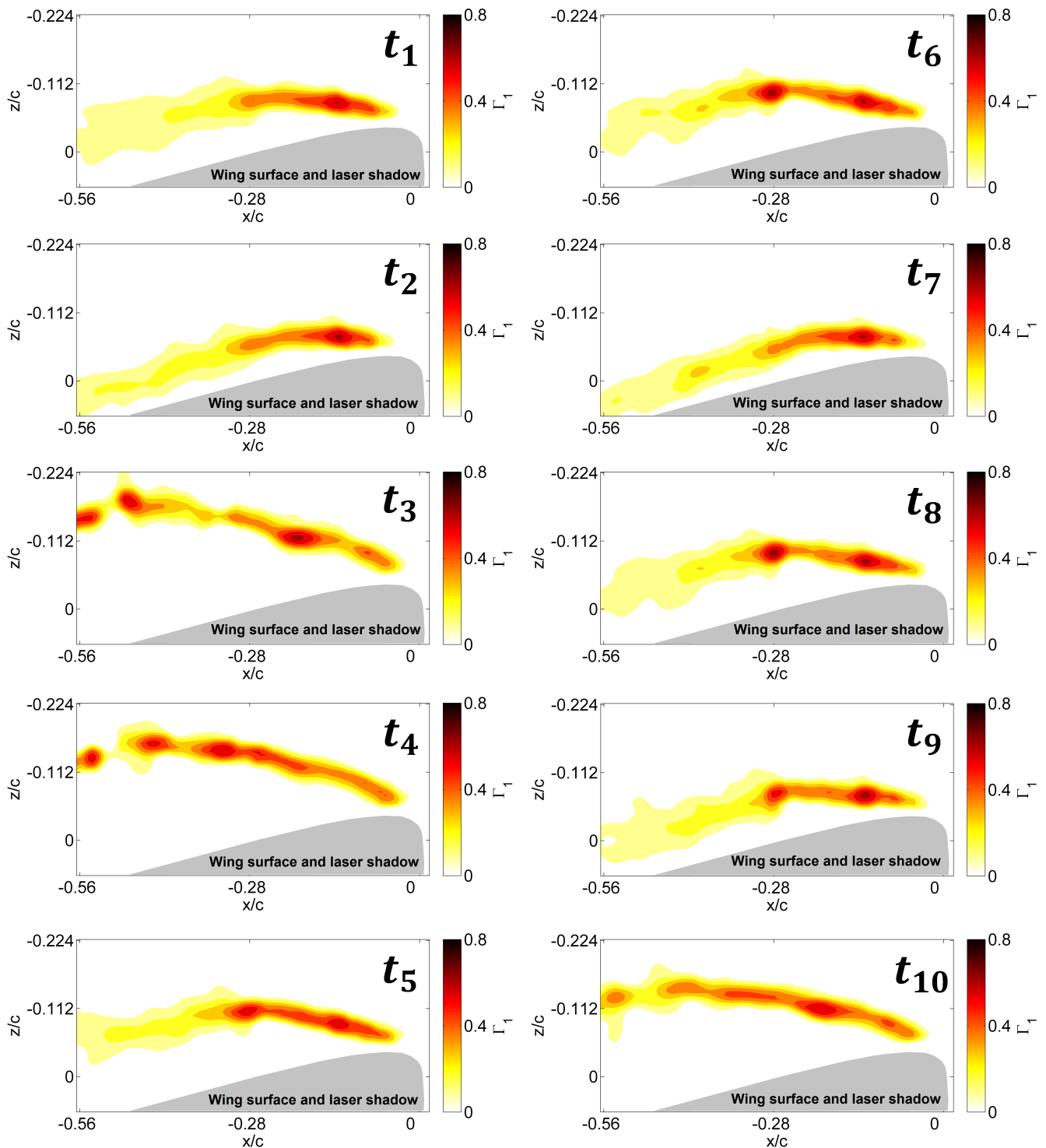


Fig. 6 Oscillatory behavior of the vortex illustrated via Γ_1 contours applied to the POD reconstructed flow field at $r/R = 0.6$, $\psi = 270^\circ$ and $\mu = 0.36$. Here, t_1, t_2, t_3 indicate consecutive phase-locked snapshots of the rotor rotation. Wing and laser shadow shown in gray

have to be first quantified. The phase-locking error was quantified by analyzing the position of the blade in each SPIV image captured and the root mean square (RMS) error in the position of the wing was less than 0.26% of the chord length. The cycle-to-cycle variations in the onset flow field was computed by standard deviation of the velocity measured at $\psi = 270^\circ$ when the wing was located at $\psi = 225^\circ$. The standard deviation of the onset flow field conditions was of the order of 0.10–0.17 m/s (2.15–2.28% based on U_∞) which indicates an insignificant cycle-to-cycle variation in the onset flow conditions. The above analysis isolates the cycle-to-cycle variations observed over the surface of the wing from variations in the onset effective freestream. Hence, any variations observed in the DSV should be due to the unsteady nature of the three-dimensional flow field rather than due to the influence of experimental artifacts.

Circulation around the vortical structure was chosen as the metric to evaluate the CTC of the DSV, which is typically proportional the amount of dynamic lift observed during the DS event. This circulation around a velocity field is defined as the amount of vorticity flux in it and was computed by evaluating Stokes theorem numerically:

$$\Gamma_V = \iint_S \omega \cdot dS = \sum_S \omega \, dx dy \quad (2)$$

where ω is vorticity and S is a closed surface chosen such that it surrounded the vortical structure observed from the NAM plots. The circulation magnitude is then non-dimensionalized as $\Gamma_V^* = \Gamma_V / cU_e$, where U_e is the effective velocity at the blade section ($r/R = 0.6$).

As mentioned earlier, the circulation around the vortex is an indication of the amount of dynamic lift observed during dynamic stall. Fig. 7a summarizes the circulation around vortex obtained in the phase-averaged velocity field. The variation of circulation around the vortex with azimuthal angle does not illustrate a typically expected variation with a prominent peak, followed by a sharper drop. This anomaly is reconciled by computing the average of instantaneous velocity field circulation computations to compare against phase-averaged circulation as illustrated in Fig. 7b. The integration contour chosen for the instantaneous velocity field encircled every vortex core in the instantaneous velocity field. The average of the instantaneous circulation exhibits the expected behavior with a maximum value at around the completion of upstroke motion of the blade ($\sim \psi = 270^\circ$). Essentially, critical information in the

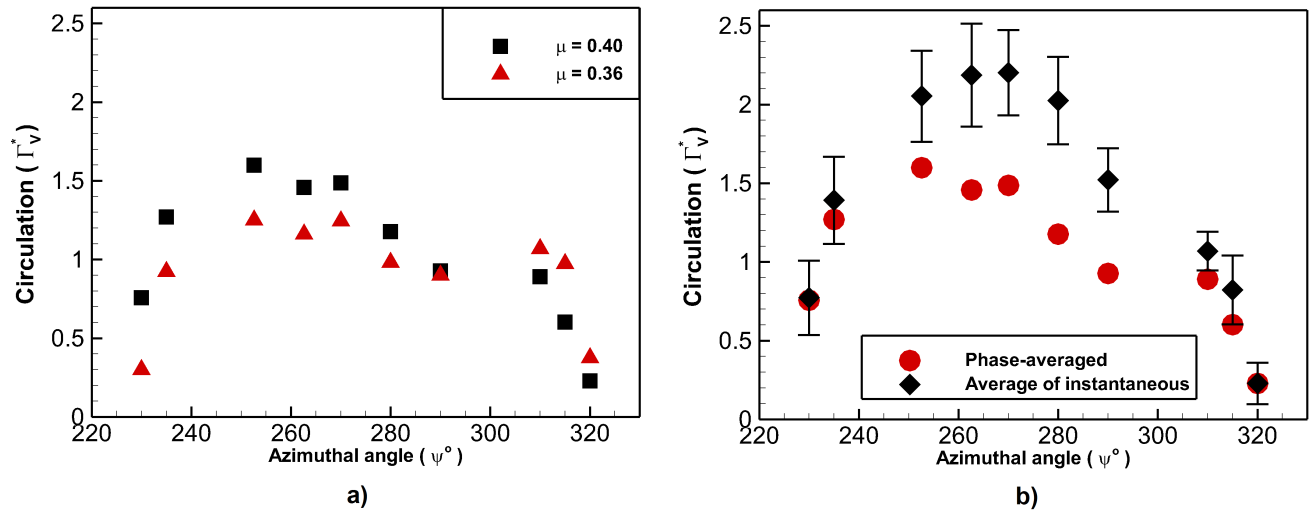


Fig. 7 Variation of the circulation of the vortex on the upper surface of the blade with azimuthal angle: a) Circulation obtained from phase-averaged velocity field, b) Comparison of circulation obtained from phase-averaged and that obtained by averaging the instantaneous circulations at $\mu = 0.40$ and $r/R = 0.6$.

instantaneous velocity fields is lost by phase-averaging during the DS event. Given, the high reduced frequency conditions, the sectional lift-coefficient (calculated using the circulation values in this work) is not expected to match data reported in prior work using oscillating airfoils and wings. Due to lack of force and moment measurements on rotating wings in dynamic stall at similar Reynolds numbers and reduced frequency conditions, direct comparisons are not possible.

Dynamic reattachment

The last part of the DS event is the phase of reattachment when the blade undergoes the down stroke motion via a reduction in pitch angle. At a sufficiently low blade pitch angle, the angle of attack is conducive for the initiation of the reattachment phase. For the flow conditions investigated in this work, reattachment is characterized as the event when the flow at the leading-edge is observed to be not separated. Analogous to dynamic separation, reattachment was also observed to be greatly affected by the advance ratio conditions. As observed in the previous sections, the dynamic stall vortex shrunk in size after reaching it's peak at around $\psi = 270^\circ$. Furthermore, reattachment was observed to occur between $315^\circ \leq \psi \leq 320^\circ$ depending on the radial location and advance ratio conditions.

Although the process of dynamic reattachment has received little attention, it is of primary importance because the lift and pitching moment hysteresis loops are strongly dependent on this phase. A few studies which have addressed the issue of dynamic reattachment [32, 33] study the flow field details during the process of reattachment on an oscillating airfoil. These studies indicate a general trend in the process of dynamic reattachment that begins at the leading-edge and progresses to the trailing-edge. However, Ahmed [32] observed a localized separation bubble after the primary reattachment point. It should be noted that Ahmed's experiments were conducted at a Mach number of 0.3 where the effects of compressibility are *not* negligible.

In contrast to prior flow field observations, in this work dynamic reattachment was not observed to begin at the leading-edge and progress to the trailing edge. Analysis of the reattachment flow fields indicates a locally separated zone close to the leading-edge and an attached flow beyond that zone as illustrated in Fig. 8. At $\psi = 315^\circ$ a large pocket of localized separation at the leading-edge is observed, while at $\psi = 320^\circ$ this pocket has reduced in size indicating a progression in reattachment. However, at the writing of this paper the exact mechanism of flow reattachment is unknown and requires further investigation.

Fig. 8 also illustrates the effect of advance ratio on the process of dynamic reattachment. Clearly an increase in advance ratio reduces the extent of separation i.e. further progress in dynamic reattachment is observed. It should be noted that the extent of dynamic separation at the beginning of the DS event increased with advance ratio, while during reattachment phase an increase in advance ratio aids reattachment.

Discussion

In this section the main results of this work are summarized in three main sections corresponding to the phases of the DS event. The three phases are also discussed with respect to helicopter performance during a DS event.

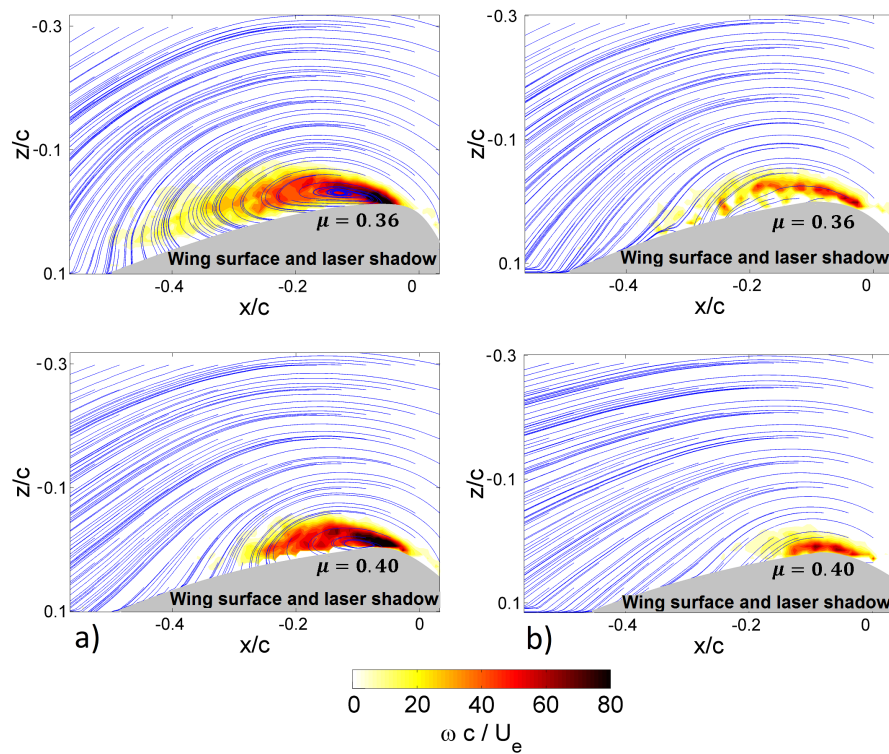


Fig. 8 Streamlines of the flow field overlaid on iso-vorticity contours during the reattachment phase: a) $\psi = 315^\circ$ and b) $\psi = 320^\circ$

Dynamic separation

The azimuth for dynamic separation (defined in this work as evidence of leading-edge separation) was determined to occur between $225^\circ \leq \psi \leq 230^\circ$. The phase-averaged PIV measurements revealed that the mechanism of separation in action was the classical trailing edge separation mechanism. Separation was first observed at the trailing edge, which then progressed up to the leading-edge before complete onset of leading-edge separation. Analysis of the dynamic separation event using phase-averaged velocity fields for two advance ratios helped characterize the general behavior of dynamic separation. At a given radial location, the separation was observed to occur at an earlier azimuth for the case of a higher advance ratio. The higher advance ratio results in a decrease in Reynolds number and an increase in reduced frequency, the coupled effects of such a change could be the reason for the earlier separation observed. The main implication for helicopter performance is the dependence of the extent of azimuthal range of DS event on advance ratio, the larger the azimuthal range of the DS event the performance is likely to deteriorate.

Moreover, cycle-to-cycle variations were observed in the instantaneous velocity fields to an extent where certain instances had no indication of separation, while others showed clear evidence of separated flow. Hence, the phase-averaged velocity fields only provide a general indication of the behavior of the flow field and the observed separation mechanism. Instantaneous velocity field analysis is necessary to develop a systematic representation of this unsteady event. These cycle-to-cycle variations indicate that even in steady forward flight conditions the onset of DS event is highly unpredictable and hence there is a need to identify exact cause of these variations. A hypothesis to consider for future investigations is the effect of the radial pressure gradient on the cycle-to-cycle variations observed in the dynamic separation event. The main implication here is that to further understand the dynamic stall event, future investigations need to incorporate rotating blades.

Dynamic stall event

Normalized angular momentum was applied to phase-averaged velocity fields to detect the DSV and characterize its behavior. Following dynamic separation the vortex appears elongated and pinned to the surface of the blade at around $\psi = 235^\circ$. As the azimuthal angle increases the vortex lifts off the blade

surface and reaches its peak height above the blade surface at $\psi = 270^\circ$. Beyond $\psi = 270^\circ$ the blade undergoes the down stroke motion and vortex proceeds to descend towards the blade surface and the separated flow finally reattaches. One other critical inference from the phase-averaged velocity fields is the unsteady nature of the flow field. The NAM fields between $250^\circ \leq \psi \leq 280^\circ$ indicate a maximum value of NAM at several x/c locations within the phase-averaged vortex. This fact indicates that the CTC variations is quite significant and hence the phase-averaged vortex presents itself as a spatially diffused vortex with multiple maximas. Again a clear trend is observed with respect to the magnitude of the CTC variations with azimuthal angle. As the angle increases the CTC variations appear to increase up to an angle $\psi = 270^\circ$, it then proceeds to decrease. These CTC variations will have significant effects on the pitching moment, since the effective center of the vortex occurs at different locations in every cycle.

Velocity field measurements acquired using Stereoscopic PIV allowed for an interpretation of the radial flow during dynamic stall event. Evidently, radial flow (corrected for span-wise flow induced due to yaw) is significant only in the separated flow regions. The separated flow region moves slower than the freestream and is hence greatly affected by the reactive centrifugal forces. This is convincing evidence that the separated flow region on a rotating blade typically has a significant radial flow (induced due to centrifugal forces) from the root to the tip of the blade. This raises questions regarding the span-wise propagation of dynamic stall on a rotating blade since there is significant transport of momentum in the radial direction. The radial flow is expected to play a significant role in the propagation of dynamic separation as well as reattachment. Further analysis of the span-wise (radial) vorticity transport in the flow field is necessary to clearly understand the role of radial flow on the DS event.

CTC variations of the dominant flow structure at $\psi = 270^\circ$ were studied using proper orthogonal decomposition (POD). POD analysis suggested that a variation in advance ratio does not effect the energy content of the higher modes, however, the lower modes (higher energy levels) show a moderate change (5-10%). Essentially, a variation in advance ratio affects only the dominant flow structures rather than the finer scale flow structures which are associated with higher modes (lower energy levels). The velocity fields were reconstructed using first 3 eigenmodes ($\sim 35\%$ of total energy). The shear layer in the approximated flow is observed to exhibit "oscillations". However, this oscillatory nature of the shear layer ("jitter" of the vortex) disappears at low advance ratios and at inboard locations (not shown here).

The physical mechanism for this behavior is unknown at the writing of this paper. Several hypotheses among others include: a) Vortex breakdown initiation at radially outboard locations due to reduction of the bulk radial flow and b) interaction between blade and tip vortices (from prior rotations) could cause the observed fluctuations in the shear layer.

CTC variations of the DSV were quantified by first computing the circulation around the vortex observed in the phase-averaged velocity fields. This was compared to circulation computed in each instantaneous velocity field and then averaged. The comparisons suggest that critical information in the instantaneous velocity fields is lost by phase-averaging during the DS event.

Dynamic reattachment

In this work dynamic reattachment was observed to occur between $315^\circ \leq \psi \leq 320^\circ$ depending on the radial location and advance ratio conditions. In contrast to prior flow field observations, in this work dynamic reattachment was not observed to begin at the leading-edge and progress to the trailing edge. Analysis of the reattachment flow fields indicate a locally separated zone close to the leading-edge and an attached flow beyond that zone. Further analysis of the time-scales for reattachment is necessary to compare dynamic reattachment in this study to regular oscillating airfoil/wing studies. Moreover, an increase in advance ratio reduces the extent of separation i.e. advances the observed dynamic reattachment phase. It should be noted that the extent of dynamic separation at the beginning of the DS event increased with advance ratio, while during reattachment phase an increase in advance ratio aids reattachment.

Conclusions

In this work the velocity field over a retreating blade in dynamic stall conditions was measured using SPIV to identify the azimuthal extent of the dynamic stall (DS) event on a rotating blade in steady forward flight condition. The main objective of this work was to study the variations in life-cycle of DS with advance ratio. First, the onset of DS via dynamic separation was studied. Second, the life-cycle of the DS event on the rotating blade was investigated. Furthermore, the cycle-to-cycle (CTC) variations in the dynamic stall event due to the unsteady nature of the flow field is studied and quantified. Finally, the

last phase of the DS event dynamic reattachment was also investigated. A summary of the results and discussion are summarized below:

- 1) The classical trailing edge separation mechanism preceded complete separation from the leading-edge. Moreover, the earlier separation as advance ratio increased, is consistent with the associated lower Reynolds number and higher reduced frequency.
- 2) CTC differences in the instance of separation were present, even though the external flow field had negligible cycle to cycle differences. This points towards other possible dynamic separation mechanisms in action and that future experiments in understanding dynamic stall should incorporate rotating blades (to capture the effect of radial pressure gradient) instead of two-dimensional oscillating airfoils.
- 3) Following separation the vortex appears elongated and pinned to the surface of the blade, then lifting off the blade surface and reaching peak height at $\psi = 270^\circ$ then descending towards the surface of the blade until reattachment. This observation is accompanied by cycle to cycle variations which were observed to increase until $\psi = 270^\circ$ and then decrease.
- 4) Radial flow (corrected for span-wise flow induced due to yaw) is significant in the separated flow regions, from the root to the tip of the blade. The radial momentum transport due to centrifugal effects could play a strong role in the propagation of dynamic stall on a rotating blade.
- 5) Variation in advance ratio affects the dominant flow structures greatly than the fine-scale structures of the flowfield.
- 6) The shear layer in the approximated reconstructed flow is observed to exhibit “oscillations”. The oscillations (vortex “jitter”) disappear at low advance ratios and at inboard locations.
- 7) In these experiments, separation initiated at $225^\circ \leq \psi \leq 230^\circ$ and reattachment occurred between $315^\circ \leq \psi \leq 320^\circ$ depending on the advance ratio conditions.
- 8) Reattachment did not begin at the leading-edge and progress to the trailing edge. Analysis of the reattachment flow fields indicates a locally separated zone close to the leading-edge and an attached

flow beyond that zone. Furthermore, an increase in advance ratio was observed to advance the dynamic reattachment phase.

Acknowledgements

This work was funded by the Army Research Office (ARO). Grant No. W911NF1010398, the technical monitor being Dr. Bryan Glaz. The authors would like to thank Alex Forbes, Brandon Liberi, and Sorin Pirau for help with conducting the experiments, Nicholas Motahari for post processing of the data and Dhwani Shukla for help with the revised figures.

References

- ¹McCroskey, W., Carr, L., and McAlister, K., "Dynamic Stall Experiments on Oscillating Airfoils," *AIAA Journal*, Vol. 14, (1), 1976, pp. 57–63.
- ²Carr, L., "Progress in Analysis and Prediction of Dynamic Stall," *Journal of aircraft*, Vol. 25, (1), 1988, pp. 6–17.
- ³Carta, F., "Dynamic Stall of Swept and Unswept Oscillating Wings," Technical report, DTIC Document, 1985.
- ⁴Lorber, P., "Dynamic Stall of Sinusoidally Oscillating Three-Dimensional Swept and Unswept Wings in Compressible Flow," AHS, Annual Forum, 48 th, Washington, Proceedings., Vol. 2, 1992.
- ⁵McCroskey, W. and Yaggy, P., "Laminar Boundary Layers on Helicopter Rotors in Forward Flight," *AIAA JOURNAL*, Vol. 6, 1968, pp. 1919–1926.
- ⁶Ham, N. D. and Young, M., "Torsional Oscillation of Helicopter Blades due to Stall," *Journal of Aircraft*, Vol. 3, (3), 1966, pp. 218–224.
- ⁷McCroskey, W. and Fisher, R. K., "Detailed Aerodynamic Measurements on a Model Rotor in the Blade Stall Regime," *Journal of the American Helicopter Society*, Vol. 17, (1), 1972, pp. 20–30.
- ⁸Bousman, W. G., "A Qualitative Examination of Dynamic Stall from Flight Test Data," *Journal of the American Helicopter Society*, Vol. 43, (4), 1998, pp. 279–295.

- ⁹Butterfield, C. P., “Aerodynamic Pressure and Flow-Visualization Measurement from a Rotating Wind Turbine Blade,” Technical report, Solar Energy Research Inst., Golden, CO (USA), 1988.
- ¹⁰Schreck, S. and Robinson, M., “Blade Three-Dimensional Dynamic Stall Response to Wind Turbine Operating Condition,” *Journal of Solar Energy Engineering*, Vol. 127, 2005, pp. 488–495.
- ¹¹Raffel, M., Kompenhans, J., and Wernert, P., “Investigation of the Unsteady Flow Velocity Field Above an Airfoil Pitching Under Deep Dynamic Stall Conditions,” *Experiments in Fluids*, Vol. 19, (2), 1995, pp. 103–111.
- ¹²Geissler, W. and Haselmeyer, H., “Investigation of Dynamic Stall Onset,” *Aerospace science and technology*, Vol. 10, (7), 2006, pp. 590–600.
- ¹³Mulleners, K. and Raffel, M., “The Onset of Dynamic Stall Revisited,” *Experiments in fluids*, Vol. 52, (3), 2012, pp. 779–793.
- ¹⁴Fujisawa, N. and Shibuya, S., “Observations of Dynamic Stall on Darrieus Wind Turbine Blades,” *Journal of Wind Engineering and Industrial Aerodynamics*, Vol. 89, (2), 2001, pp. 201–214.
- ¹⁵Ferreira, C. S., van Kuik, G., van Bussel, G., and Scarano, F., “Visualization by PIV of Dynamic Stall on a Vertical Axis Wind Turbine,” *Experiments in Fluids*, Vol. 46, (1), 2009, pp. 97–108.
- ¹⁶Harbig, R., Sheridan, J., and Thompson, M., “Reynolds number and aspect ratio effects on the leading-edge vortex for rotating insect wing planforms,” *Journal of Fluid Mechanics*, Vol. 717, 2013, pp. 166–192.
- ¹⁷Garmann, D. J., Visbal, M. R., and Orkwis, P. D., “Three-dimensional flow structure and aerodynamic loading on a revolving wing,” *Physics of Fluids (1994-present)*, Vol. 25, (3), 2013, pp. 034101.
- ¹⁸DiOttavio, J., Watson, K., Cormey, J., Komerath, N., and Kondor, S., “Discrete Structures in the Radial Flow Over a Rotor Blade in Dynamic Stall,” Proceedings of the 26th applied aerodynamics conference, AIAA, Honolulu, Hawaii, USA, 2008.
- ¹⁹Raghav, V. and Komerath, N., “An Exploration of Radial Flow on a Rotating Blade in Retreating Blade Stall,” *Journal of the American Helicopter Society*, Vol. 58, (2), 2013, pp. 1–10.
- ²⁰Raghav, V. and Komerath, N., “Velocity Measurements on a Retreating Blade in Dynamic Stall,” *Experiments in Fluids*, Vol. 55:1669, 2014, pp. 1–10.

²¹Raghav, V., Mayo, M., Lozano, R., and Komerath, N., “Evidence of vortex-induced lift on a yawed wing in reverse flow,” *Proceedings of the Institution of Mechanical Engineers, Part G: Journal of Aerospace Engineering*, Vol. 228, (11), 2013, pp. 2130–2137.

²²McAlister, K., Pucci, S., McCroskey, W., and Carr, L., “An Experimental Study of Dynamic Stall on Advanced Airfoil Sections. Volume 2. Pressure and Force Data.” Technical report, DTIC Document, 1982.

²³Raffel, M., Willert, C. E., and Kompenhans, J., *Particle Image Velocimetry: A Practical Guide*, Springer, 1998.

²⁴Raghav, V., *Radial Flow Effects on a Retreating Rotor Blade*, Ph.D. thesis, Georgia Institute of Technology, 2014.

²⁵Lawson, N. and Wu, J., “Three-dimensional Particle Image Velocimetry: Experimental Error Analysis of a Digital Angular Stereoscopic System,” *Measurement Science and Technology*, Vol. 8, (12), 1997, pp. 1455.

²⁶Carr, L. and Chandrasekhara, M., “Compressibility Effects on Dynamic Stall,” *Progress in Aerospace Sciences*, Vol. 32, (6), 1996, pp. 523–573.

²⁷Van Dommelen, L. and Shen, S., “The Genesis of Separation,” *Symposium on Numerical and Physical Aspects of Aerodynamic Flows*, 1982.

²⁸Graftieaux, L., Michard, M., and Grosjean, N., “Combining PIV, POD and Vortex Identification Algorithms for the Study of Unsteady Turbulent Swirling Flows,” *Measurement Science and Technology*, Vol. 12, (9), 2001, pp. 1422.

²⁹Ol, M. V., Bernal, L., Kang, C.-K., and Shyy, W., “Shallow and deep dynamic stall for flapping low Reynolds number airfoils,” *Animal Locomotion*, Springer, 2010, pp. 321–339.

³⁰Aubry, N., Guyonnet, R., and Lima, R., “Spatiotemporal Analysis of Complex Signals: Theory and Applications,” *Journal of Statistical Physics*, Vol. 64, (3-4), 1991, pp. 683–739.

³¹Sirovich, L., “Turbulence and the Dynamics of Coherent Structures. I-Coherent Structures. II-Symmetries and Transformations. III-Dynamics and Scaling,” *Quarterly of applied mathematics*, Vol. 45, 1987, pp. 561–571.

³²Ahmed, S. and Chandrasekhara, M., "Reattachment Studies of an Oscillating Airfoil Dynamic Stall Flowfield," *AIAA journal*, Vol. 32, (5), 1994, pp. 1006–1012.

³³Green, R. and Galbraith, R. M., "Dynamic Recovery to Fully Attached Aerofoil Flow From Deep Stall," *AIAA journal*, Vol. 33, (8), 1995, pp. 1433–1440.

Table 1. High advance ratio facility
rotor specifications

Description	Value
Rotor blade airfoil section	NACA0013
Blade span	0.622 m
Blade chord	0.178 m
Blade aspect ratio	3.49
Rotor disc radius	0.889 m
Solidity	0.0895
Height	1.4 m
Precone	1.6 deg
Maximum collective	10 deg
Maximum cyclic	6.5 deg
Maximum TPP tilt	16 deg
Motor power	3.73 kW

Table 2. Reynolds number, reduced frequency and angle of attack at each flow condition for $r/R = 0.6$ measurement location, where the subscripts indicate the advance ratio

ψ	$Re_{0.36}$	$Re_{0.40}$	$k_{0.36}$	$k_{0.40}$	$\alpha_{0.36}$	$\alpha_{0.40}$
230 °	68533	62056	0.31	0.34	16.49 °	17.70 °
235 °	64492	57566	0.33	0.37	16.92 °	18.27 °
252.6 °	54212	46144	0.39	0.46	18.13 °	19.97 °
262.6 °	51364	42979	0.41	0.49	18.50 °	20.54 °
270 °	50730	42275	0.42	0.5	18.59 °	20.67 °
280 °	51886	43560	0.41	0.49	18.43 °	20.43 °
290 °	55319	47374	0.38	0.45	17.99 °	19.77 °
310 °	68533	62056	0.31	0.34	16.49 °	17.70 °
315 °	73018	67039	0.29	0.32	16.03 °	17.12 °
320 °	77912	72477	0.27	0.29	15.55 °	16.53 °

Table 3. Summary of velocity uncertainty estimates

Type	Error
In-plane random error	0.074–0.252 px
In-plane bias error	0.01 m/s
Lag Error	Insignificant
In-plane measurement error ($\%U_p$)	0.4%–1.2%
Out-of-plane measurement error ($\%W_p$)	0.58%–3.08%